

Optimal β -beam at the CERN-SPS

J. Burguet-Castell ^a, D. Casper ^b, E. Couce ^a, J.J. Gómez-Cadenas ^a,
P. Hernández ^a

^a IFIC, Universidad de València, E-46100 Burjassot, Spain

^b Department of Physics and Astronomy, University of California, Irvine, CA 92697-4575, USA

Received 14 March 2005; received in revised form 14 June 2005; accepted 20 June 2005

Available online 11 August 2005

Abstract

A β -beam with maximum $\gamma = 150$ (for ${}^6\text{He}$ ions) or $\gamma = 250$ (for ${}^{18}\text{Ne}$) could be achieved at the CERN-SPS. We study the sensitivity to θ_{13} and δ of such a beam as function of γ , optimizing with the baseline constrained to CERN–Frejus (130 km), and also with simultaneous variation of the baseline, for a fixed ion flux. These results are compared to the *standard* scenario previously considered, with lower $\gamma = 60/100$, and also with a higher $\gamma \sim 350$ option that requires a more powerful accelerator. We conclude that the sensitivity to CP violation and θ_{13} increases significantly with γ if the baseline is increased proportionally, while for the CERN–Frejus scenario the dependence on γ is mild provided γ is above 100.

© 2005 Elsevier B.V. All rights reserved.

1. Introduction

Results from atmospheric [1], solar [2], reactor [3] and long-baseline [4] neutrino experiments in recent years can be economically accommodated in the Standard Model (SM) with neutrino masses and a three-neutrino mixing matrix [5]. In this case, the lepton sector of the SM closely resembles that of the quarks and there are new physical parameters measurable at low energies: the three neutrino masses, m_i ($i = 1, 2, 3$), three mixing angles,

E-mail addresses: jordi.burguet.castell@cern.ch (J. Burguet-Castell), dcasper@uci.edu (D. Casper), ecouce@gmail.com (E. Couce), gomez@mail.cern.ch (J.J. Gómez-Cadenas), pilar.hernandez@ific.uv.es, pilar.hernandez@cern.ch (P. Hernández).

θ_{ij} ($i \neq j = 1, 2, 3$), and a CP-violating phase, δ . In contrast with the quark sector, two additional phases could be present if neutrinos are Majorana. Of these new parameters, present experiments have determined just two neutrino mass-square differences and two mixing angles: ($|\Delta m_{23}^2| \simeq 2.2 \times 10^{-3} \text{ eV}^2$, $\theta_{23} \simeq 45^\circ$) which mostly drive the atmospheric oscillation and ($\Delta m_{12}^2 \simeq 8 \times 10^{-5} \text{ eV}^2$, $\theta_{12} \simeq 32^\circ$) which mostly drive the solar one. The third angle, θ_{13} , as well as the CP-violating phases (δ , and possible Majorana phases) remain undetermined. Only an upper limit $\theta_{13} \leq 12^\circ$ is known. Another essential piece of information needed to clarify the low-energy structure of the lepton flavor sector of the SM is the neutrino mass hierarchy and the absolute neutrino mass scale. The former is related to the sign of the largest mass-square difference (Δm_{23}^2), which determines if the spectrum is hierarchical (if the two most degenerate neutrinos are lighter than the third one) or degenerate (if they are heavier).

Measurement of some of these parameters may be possible in high-precision neutrino-oscillation experiments. A number of experimental setups to significantly improve on present sensitivity to θ_{13} , δ and the sign of Δm_{23}^2 have been discussed in the literature: neutrino factories (neutrino beams from boosted-muon decays) [6–8], superbeams (very intense conventional neutrino beams) [9–12], improved reactor experiments [13] and more recently β -beams (neutrinos from boosted-ion decays) [14,15]. These are quite different in terms of systematics but all face a fundamental problem which limits the reach of each individual experiment significantly, namely the correlations and degeneracies between parameters [16–24]; θ_{13} and δ must be measured simultaneously, and other oscillation parameters are not known with perfect precision.

To resolve these degeneracies it is important to measure as many independent channels as possible and to exploit the energy and/or baseline dependence of the oscillation signals and matter effects in neutrino propagation. In many cases, the best way to do this is by combining different experiments; indeed the synergies between some combinations of the setups mentioned above have been shown to be considerable.

The neutrino factory provides ultimate sensitivity to leptonic CP violation, and thus represents the last step on a long-term road map to reveal the lepton-flavor sector of the SM. Recently it was shown that a β -beam running at a higher γ than previously considered (and longer baselines), in combination with a massive water detector, can reach sensitivity to leptonic CP violation and $\text{sign}(\Delta m_{23}^2)$ that competes with a neutrino factory's. The optimal setup among those considered in [26] was a β -beam with $\gamma = 350/580$ for ${}^6\text{He}$ and ${}^{18}\text{Ne}$ isotopes respectively and a baseline $L \simeq 730 \text{ km}$. If constructed at CERN, this beam would require a refurbished SPS or an acceleration scheme utilizing the LHC—implying substantial R&D effort in either case.

This paper considers instead the possibility of using the existing CERN-SPS up to its maximum power, allowing a beam with $\gamma = 150$ (250) for ${}^6\text{He}$ (${}^{18}\text{Ne}$) ions (some preliminary results of this study were presented in [27]). The design of this β -beam is essentially as described in [28].

The advantages of increasing the γ factor discussed in [26] also apply in this case. The oscillation signals grow at least linearly with the γ factor, therefore the highest γ possible is preferred in principle, if the baseline is adjusted appropriately. Furthermore when the

energy is well above the Fermi momentum of the target nuclei, energy dependence of the oscillation signals is very effective in resolving parameter degeneracies. In practice there are two caveats to this rule. First, water Cherenkov detectors are best suited for quasi-elastic (QE) reactions, where the neutrino energy can be kinematically reconstructed. Therefore, sensitivity improves with γ only until the inelastic cross-section begins to dominate; we will show that this occurs for $\gamma \geq 400$. The second concern is background, since NC single-pion production can mimic the appearance signal; it is demonstrated in [26] and confirmed here that this background is manageable, even for $\gamma > 100$.

More concretely the purpose of this paper is two-fold. First, optimization of a CERN-SPS β -beam by answering the following questions:

- Assuming an underground laboratory at Frejus with a megaton water Cherenkov detector, what is the optimal γ with the existing CERN-SPS?
- For the maximum γ achievable with the CERN-SPS, what is the optimal β -beam baseline?
- Is there any physics advantage to varying the γ ratio for ${}^6\text{He}$ and ${}^{18}\text{Ne}$, i.e., a ratio different from $\gamma_{18\text{Ne}}/\gamma_{6\text{He}} = 1.67$ (which allows both beams to circulate simultaneously) [29]?

Second, comparing the performance of the following set-ups:

- Setup I: $L = 130$ km (CERN–Frejus) at the optimal γ accessible to the CERN-SPS.
- Setup II: $\gamma = 150$ at the optimal baseline.
- Setup III: $\gamma = 350$ at $L = 730$ km, which is a symmetric version of the configuration considered in [26]. To accelerate the ions would require either a refurbished SPS (with superconducting magnets) or a more powerful accelerator, such as the Tevatron or LHC.

In all cases an intensity of 2.9×10^{18} ${}^6\text{He}$ and 1.1×10^{18} ${}^{18}\text{Ne}$ decays per year [28] and an integrated luminosity corresponding to 10 years are assumed. Although these luminosities have been estimated for simultaneous ion circulation (fixing the ratio of γ 's to 1.67) Ref. [30] argues they are achievable even if the ions circulate separately at the same γ , by injecting more bunches. While these intensities are realistic for the CERN-SPS, the same has not been demonstrated for other accelerators like the Tevatron or LHC. The far detector is a Super-Kamiokande-like water Cherenkov design, with fiducial mass 440 kton.

The paper is organized as follows. Section 2 shows expected fluxes and event rates for the maximum γ achievable at the CERN-SPS. Section 3 describes the performance of a large water Cherenkov detector for the appearance and disappearance signals and estimates the atmospheric background, an important constraint in design of the bunch length. Section 4 deals with optimizations needed to define setups I and II and Section 5 compares the physics reach of the three emergent reference setups. Section 6 discusses our outlook and conclusions.

2. Neutrino fluxes and rates

Fig. 1 shows the fluxes for the maximum acceleration of the ions at the CERN-SPS: $\gamma = 150$ for ${}^6\text{He}$ and $\gamma = 250$ for ${}^{18}\text{Ne}$ at $L = 300$ km. Table 1 shows the rate of charged-current interactions expected per kiloton in one year.

3. Measurements at a β -beam

The parameters θ_{13} and δ are best studied by probing the appearance channels for neutrino oscillation in the atmospheric energy range: golden ($\nu_\mu \leftrightarrow \nu_e$) [7,16] and silver ($\nu_\tau \leftrightarrow \nu_e$) [24] channels have been identified. In the setups considered here, neutrino energies are below τ threshold, therefore only the golden channel is available.

The disappearance transition $\nu_e \rightarrow \nu_e$ can also be measured. This is an important complement to the golden channel measurement, because the intrinsic degeneracy [17] in the golden measurement can be resolved: the disappearance measurement depends on θ_{13} , but not on δ . The synergy between the appearance and disappearance channels for a β -beam is thus analogous to that between superbeam and reactor experiments [13].

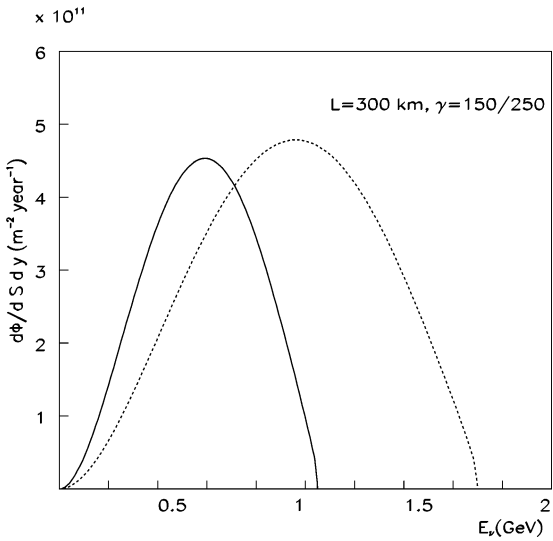


Fig. 1. $\bar{\nu}_e$ (solid) and ν_e (dashed) fluxes in $\text{m}^{-2} \text{yr}^{-1}$ as a function of the neutrino energy at $L = 300$ km for the maximum acceleration of the ${}^6\text{He}$ ($\gamma = 150$) and ${}^{18}\text{Ne}$ ($\gamma = 250$) at the CERN-SPS.

Table 1
Number of charged-current events per kton-year, in the absence of oscillation, for the maximum acceleration of ${}^6\text{He}$ and ${}^{18}\text{Ne}$ at the CERN-SPS. The average neutrino energy is also shown

γ	L (km)	$\bar{\nu}_e$ CC	ν_e CC	$\langle E_\nu \rangle$ (GeV)
150/250	300	22.8	115.6	0.58/0.94

3.1. Detection of the appearance signal

The signal for the golden transition is a charged-current event (CC) with a muon in the final state. Ref. [26] studied the performance of a 440 kton fiducial water Cherenkov detector similar to Hyper-Kamiokande or the proposed by the UNO experiment [31]. This analysis can be extended to different γ 's, using the same neutrino physics generator, detector simulation and reconstruction algorithms as described in [25,26], with realistic e – μ separation by pattern recognition, and the requirement of a delayed coincidence from muon decay.

Fig. 2 shows the reconstructed energy spectra of signal and background at maximum CERN-SPS γ , for two different values of θ_{13} . Backgrounds are smaller for ${}^6\text{He}$ than ${}^{18}\text{Ne}$, and both neutrino and anti-neutrino backgrounds tend to cluster at low energies. Most of the background reconstructs below 500 MeV.

The neutrino energy resolution depends strongly on the proportion of quasi-elastic (QE) and non-quasi-elastic (non-QE) interactions in the signal. Neutrino energy is reconstructed assuming two-body, quasi-elastic kinematics, so contamination from non-QE events introduces a bias between the true and reconstructed energies. Fig. 3 shows the fraction of QE and non-QE events passing the selection criteria. As expected the non-QE contamination is smaller for anti-neutrinos since the average beam energy is also smaller for the chosen γ 's.

To properly include both detector resolution and non-QE contamination effects, a matrix describing the migration between true and reconstructed neutrino energies is constructed. Migration matrices are also computed for the backgrounds. Given the irreducible Fermi motion and muon threshold, the first energy bin extends from 0–500 MeV and bins of 250 MeV width are used above it (note that due to the muon threshold the first bin is effectively of the same size as the others). For the high- γ setup III, the first bin is discarded.

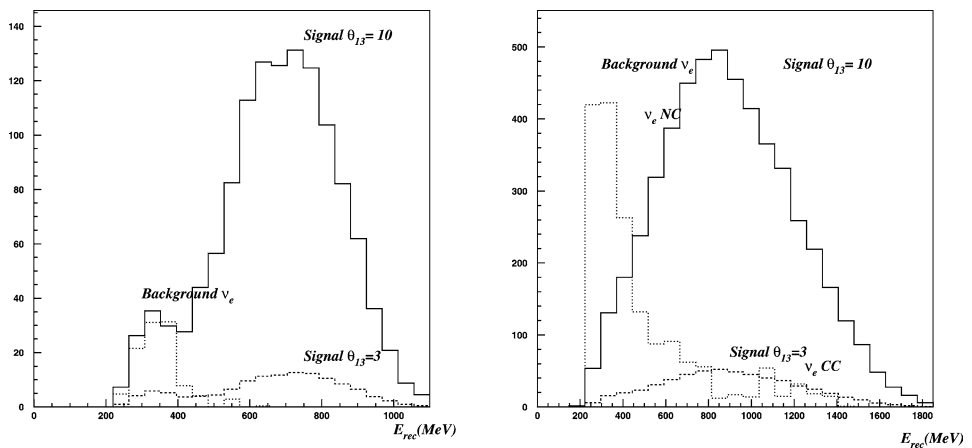


Fig. 2. Reconstructed energy for signal with $\theta_{13} = 10^\circ$ (solid) and $\theta_{13} = 3^\circ$ (dashed)) and background (dotted) at the maximum acceleration of ${}^6\text{He}$ (left) and ${}^{18}\text{Ne}$ (right) ions at the CERN-SPS. The absolute normalization corresponds to one year.

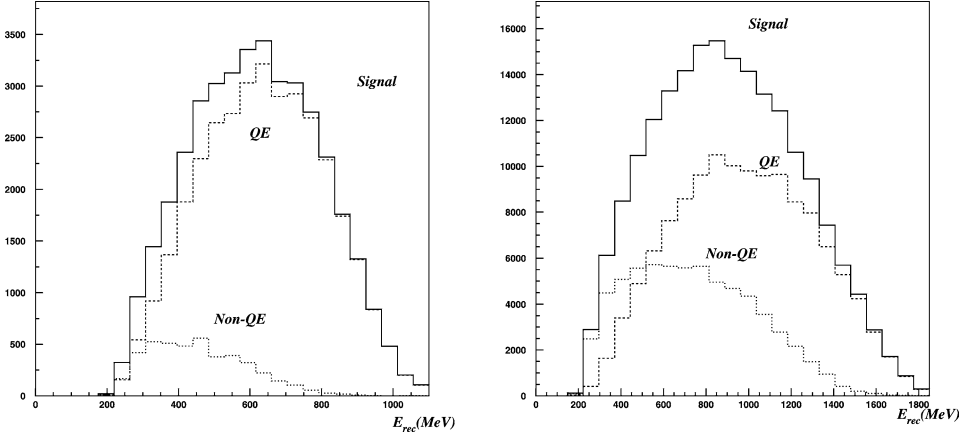


Fig. 3. Quasi-elastic and non-quasi-elastic components in the μ appearance signal for unit oscillation probability (the absolute normalization is arbitrary) at maximum CERN-SPS acceleration of ${}^6\text{He}$ (left) and ${}^{18}\text{Ne}$ (right).

Tables 3, 4 and 5 in Appendix A show these migration matrices for $\gamma = 120, 150$ and 350 for ${}^6\text{He}$ and ${}^{18}\text{Ne}$.¹ We used three bins: $0\text{--}500, 500\text{--}750$ and 750+ MeV for $\gamma = 120, 150$ and seven (of width 250 MeV above 500 MeV and of width 500 MeV above 2 GeV) for $\gamma = 350$. The efficiencies are quite high ($\sim 30\text{--}50\%$) even when the background fraction is held below 10^{-3} .

3.2. Detection of the disappearance signal

For $\nu_e \rightarrow \nu_e$ ($\bar{\nu}_e \rightarrow \bar{\nu}_e$) transitions, the signal is a CC interaction with an electron (positron) in the final state. In [26] this channel was included with a conservatively estimated 50% flat efficiency and negligible background. Since the energy resolution is also strongly affected by the non-QE contamination for this sample, this analysis is now refined to include the effect of migrations. While the background level for this large signal can be safely neglected in comparison to other systematic errors to be discussed later, a matrix of efficiencies should be used to account for the signal migrations. Tables 6 and 7 in Appendix A show these matrices for ${}^6\text{He}$ and ${}^{18}\text{Ne}$ at various γ 's. Efficiencies are quite high, especially at lower energies where they reach $80\text{--}90\%$.

3.3. Atmospheric background

An important background for any accelerator-based experiment to control arises from atmospheric neutrinos. A detector like Super-Kamiokande will expect approximately 120 $\nu_\mu + \bar{\nu}_\mu$ interactions per kiloton-year (including the disappearance of ν_μ into ν_τ). Of these, 32 atmospheric $\nu_\mu + \bar{\nu}_\mu$ per kiloton-year pass all the selection cuts (one non-showering ring, accompanied by a delayed coincidence from muon decay). The reconstructed spectrum of those events scaled by a factor $1/500$ is shown in Fig. 4 (solid line) alongside the

¹ Matrices with appropriate binning for other choices of γ can be obtained from the authors on request.

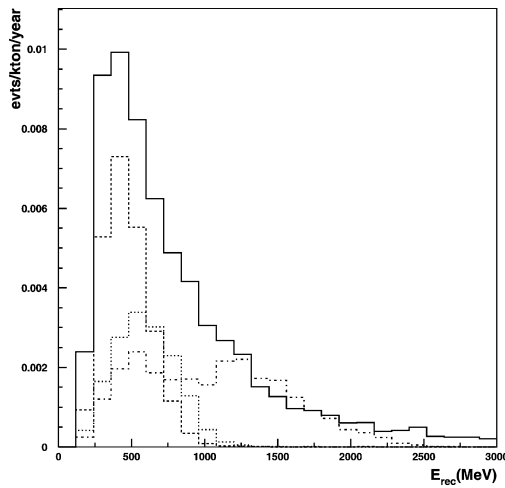


Fig. 4. Solid line: energy spectrum of atmospheric $\nu_\mu + \bar{\nu}_\mu$ background per kiloton-year, scaled down by a factor 1/500. Dashed, dotted and dash-dotted lines: energy spectrum of signal events per kiloton-year for $\gamma = 120, 150$ and 350 assuming $\theta_{13} = 1^\circ$.

Table 2

Surviving atmospheric ν_μ background per kton-year after cuts: on the high-energy end-point of the β -beam neutrino spectrum (E_{\max}), the low-energy tail (E_{\min}) for setup III, and the lepton scattering angle ($\cos \theta_l$), as described in the text

γ	Selection	E_{\max} cut	E_{\min} cut	$\cos \theta_l$ cut
120	32	19	19	15
150	32	24	24	15
350	32	30	19	5

signal for the three example setups to be considered later, namely, $\gamma = 120$ ($L = 130$ km, dashed), $\gamma = 150$ ($L = 300$ km, dotted) and $\gamma = 350$ ($L = 730$ km, dashed-dotted), assuming $\theta_{13} = 1^\circ$.

There are two additional handles to further reduce the atmospheric background. First, at a given γ , we know the end-point of the signal spectrum, and there is no efficiency penalty for excluding events above the maximum beam energy. This cut obviously works best for lower- γ scenarios. Table 2 shows the effect of the end-point cut for different γ 's. For higher γ , it is also helpful to set a *lower* energy cut. Requiring $E \geq 500$ MeV, for instance, is free for the highest $\gamma = 350$ option, since this bin is not considered in the analysis anyway.

Second, a directional cut is also possible, since the beam arrives from a specific, known direction but the atmospheric background is roughly isotropic. While the neutrino direction cannot be measured directly, it is increasingly correlated with the observable lepton direction at high energies. Fig. 5 illustrates this correlation for the three reference set-ups. Thus, a directional cut is more effective as γ increases, but is never perfectly efficient. To compare the power of this cut for the different setups, we define it to achieve a 90% efficiency in all cases: $\cos \theta_l > 0.45$ for $\gamma = 350$, $\cos \theta_l > -0.3$ for $\gamma = 150$ and $\cos \theta_l > -0.5$ for

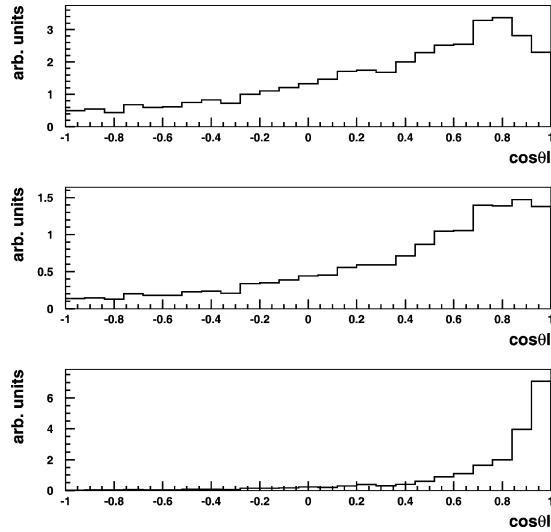


Fig. 5. Cosine of the reconstructed neutrino–lepton scattering angle for three setups: $\gamma = 120$ (top), $\gamma = 150$ (middle) and $\gamma = 350$ (bottom).

$\gamma = 120$. The remaining atmospheric background for each setup is summarized in Table 2. Thanks to the directional cut, background rejection for the highest γ is a factor three better than the alternative scenarios.

Even with energy and directional cuts, 5 to 15 atmospheric ν_μ background events per kiloton-year remain, compared to the expected intrinsic beam-induced detector background (mostly due to NC single-pion production) of $\mathcal{O}(10^{-2})$ events. To reduce atmospheric contamination to a negligible level (say ten times below the intrinsic background) would require a rejection factor $\mathcal{O}(10^4)$, although since the atmospheric background can be well measured a rejection factor 5–10 times less stringent is probably tolerable.

This rejection factor can be achieved by timing of the parent ion bunches. It is estimated [15] that a rejection factor of 2×10^4 is feasible with bunches 10 ns in length. Based on the present results, a less demanding scheme for the number of bunches and bunch length could be workable.

3.4. Systematic errors

Although a detailed analysis of all possible systematic errors is beyond the scope of this paper, we have included the two that will likely dominate. First, the uncertainty in the fiducial mass of the near and far detectors, which we estimate as a $\pm 5\%$ effect on the expected far-detector rate. Second, the uncertainty on the ratio of anti-neutrino/neutrino cross sections, which we assume a near detector can measure with an accuracy of $\pm 1\%$.²

² The calculable neutrino and anti-neutrino energy spectra of the β -beam will facilitate cross-section measurements, compared to a traditional neutrino beam.

To include these errors, two new parameters are added to the fits: A , the global normalization, and x , the relative normalization of anti-neutrino to neutrino rates. More precisely, if $n_{\mu,e}^{i,\pm}$ is the number of *measured* muon and electron events in the energy bin i for the anti-neutrino (+) or neutrino (−) beam, and $N_{\mu,e}^{i,\pm}(\theta_{13}, \delta)$ is the expected number for some values of the unknown parameters (θ_{13}, δ) , then we minimize the following χ^2 function:

$$\chi^2(\theta_{13}, \delta, A, x) = 2 \sum_{i,f=e,\mu} \left\{ Ax N_f^{i,+} - n_f^{i,+} + n_f^{i,+} \log \left(\frac{n_f^{i,+}}{Ax N_f^{i,+}} \right) \right. \\ \left. + AN_f^{i,-} - n_f^{i,-} + n_f^{i,-} \log \left(\frac{n_f^{i,-}}{AN_f^{i,-}} \right) \right\} + \frac{(A-1)^2}{\sigma_A^2} + \frac{(x-1)^2}{\sigma_x^2}, \quad (3.1)$$

where $\sigma_A = 0.05$ and $\sigma_x = 0.01$. The minimization in the parameters A and x for fixed values of θ_{13} and δ can be done analytically to leading order in the deviations $A - 1$ and $x - 1$, that is, solving the linearized system:

$$\frac{\partial \chi^2}{\partial A} = 0, \quad \frac{\partial \chi^2}{\partial x} = 0. \quad (3.2)$$

In what follows, sensitivity to the parameters (θ_{13}, δ) will be quantified using 99% confidence regions for two degrees of freedom; that is, the curves satisfying:

$$\chi^2(\theta_{13}, \delta, A_{\min}, x_{\min}) = 9.21. \quad (3.3)$$

4. Optimization of the CERN-SPS β -beam

The following sensitivity plots are used to optimize the physics performance of different β -beams:

- Sensitivity to CP violation: region on the plane (θ_{13}, δ) where the phase δ can be distinguished from both $\delta = 0^\circ$ and $\delta = 180^\circ$ for *any* best fit value of θ_{13} , at 99% confidence level or better.
- Sensitivity to θ_{13} : region on the plane (θ_{13}, δ) where the angle θ_{13} can be distinguished from $\theta_{13} = 0$ for any best fit value of δ , at 99% confidence level or better.

Unless otherwise specified, the following solar- and atmospheric-neutrino oscillation parameters are assumed:

$$\Delta m_{12}^2 = 8.2 \times 10^{-5} \text{ eV}^2, \quad \theta_{12} = 32^\circ, \\ \Delta m_{23}^2 = 2.2 \times 10^{-3} \text{ eV}^2, \quad \theta_{23} = 45^\circ. \quad (4.1)$$

4.1. Optimal γ for the CERN–Frejus baseline

One frequently considered *standard* setup adopts the CERN–Frejus baseline $L = 130$ km and $\gamma = 60/100$ for ${}^6\text{He}/{}^{18}\text{Ne}$ [15,32]. This setup appears to be far from optimal

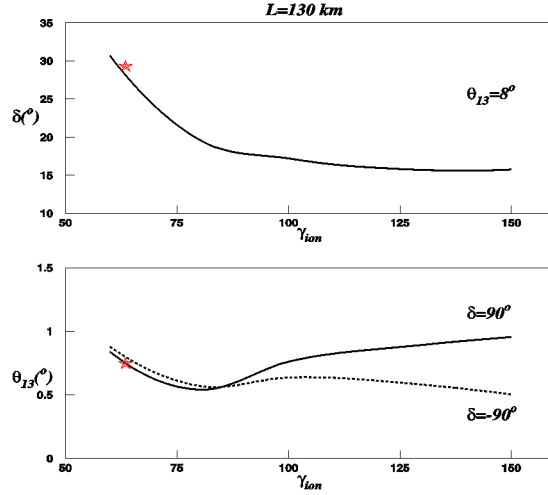


Fig. 6. Top: γ -dependence of 99% confidence level δ -sensitivity (i.e., minimum value of $\delta > 0$ that can be distinguished from $\delta = 0, 180^\circ$) at $\theta_{13} = 8^\circ$. Bottom: θ_{13} -sensitivity (minimum value of θ_{13} that can be distinguished from zero) for $\delta = +90^\circ$ (solid) and $\delta = -90^\circ$ (dashed), assuming $L = 130$ km and $\gamma_{\text{He}} = \gamma_{\text{Ne}}$. The stars indicate the values for the $\gamma = 60/100$ option in [15,32].

even if the baseline is kept fixed. As noted in [26], a higher- γ beam increases the event rate and allows the energy dependence of the signal to be analyzed. Taking the identical γ for ${}^6\text{He}$ and ${}^{18}\text{Ne}$, Fig. 6 shows the γ -dependence of the 99% CL δ and θ_{13} sensitivity, as defined above. The stars indicate the values of the previously considered setup in [15,32], corresponding to $\gamma = 60/100$. Clearly the CP-violation sensitivity is significantly better for larger γ . For $\gamma \geq 100$ the sensitivity to CP violation and θ_{13} changes rather slowly. This is not surprising, since increasing γ at fixed baseline does not reduce the flux significantly at low energies (see Fig. 7), just as for a neutrino factory. In the absence of backgrounds, there is no penalty associated with higher γ , although in practice, the non-negligible backgrounds result in a small decrease in θ_{13} sensitivity at higher γ , for some values of δ .

Although there is no unique optimal γ within the wide range $\gamma = 100$ – 150 when the baseline is fixed to $L = 130$ km, consider for illustration an intermediate $\gamma = 120$ to define setup I; a different choice of $\gamma > 100$ will not make a significant difference.

There appears to be no advantage to the asymmetric choice $\gamma_{18\text{Ne}}/\gamma_{6\text{He}} = 1.67$. The asymmetric option is always comparable in sensitivity to a symmetric one with the smaller γ of the two, so a symmetric γ configuration is adopted for setup I.

4.2. Optimal L for maximum ion acceleration $\gamma = 150$

As argued in [26], physics performance should improve with increasing γ , if the baseline is correspondingly scaled to remain close to the atmospheric oscillation maximum, due to the (at least) linear increase in rate with γ . This growth in sensitivity eventually saturates for a water detector, which becomes inefficient in reconstructing neutrino energies

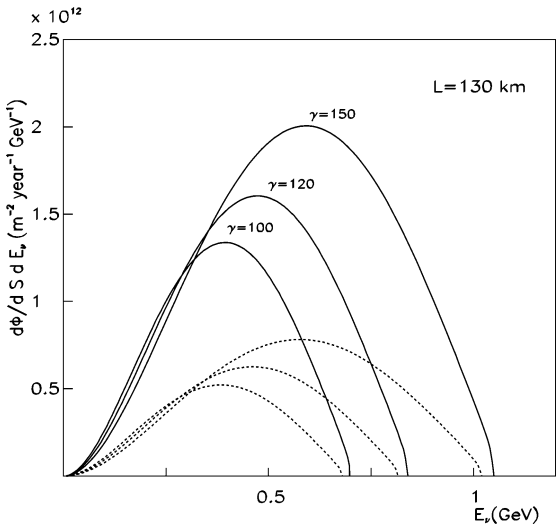


Fig. 7. Energy spectra of ν_e (dashed) and $\bar{\nu}_e$ (solid) in $m^{-2} yr^{-1} GeV^{-1}$ at $L = 130 km$ for $\gamma = 100, 120, 150$.

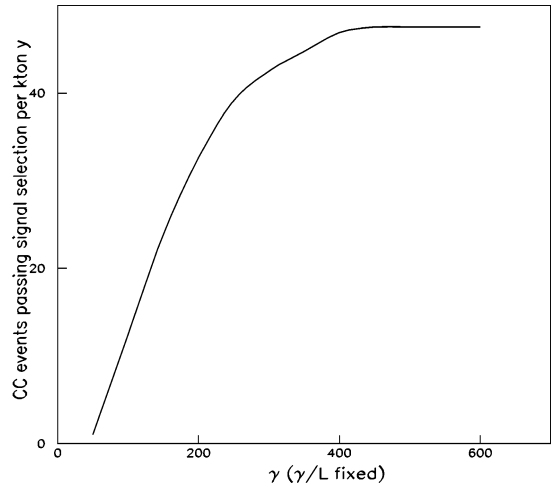


Fig. 8. Number of CC appearance candidates (from ^{18}Ne) for unit oscillation probability, as a function of γ , holding γ/L fixed.

in the inelastic regime. Fig. 8, where the number of CC appearance candidates selected (for unit oscillation probability) is plotted as a function of γ (for γ/L fixed), confirms this expectation. Saturation occurs for $\gamma \simeq 400$, above the maximum acceleration possible at the CERN-SPS, since the flux is still large in the quasi-elastic region (see Fig. 7).

Fixing γ to the CERN-SPS we next study the optimal baseline and how the symmetric γ setup compares with the asymmetric one.

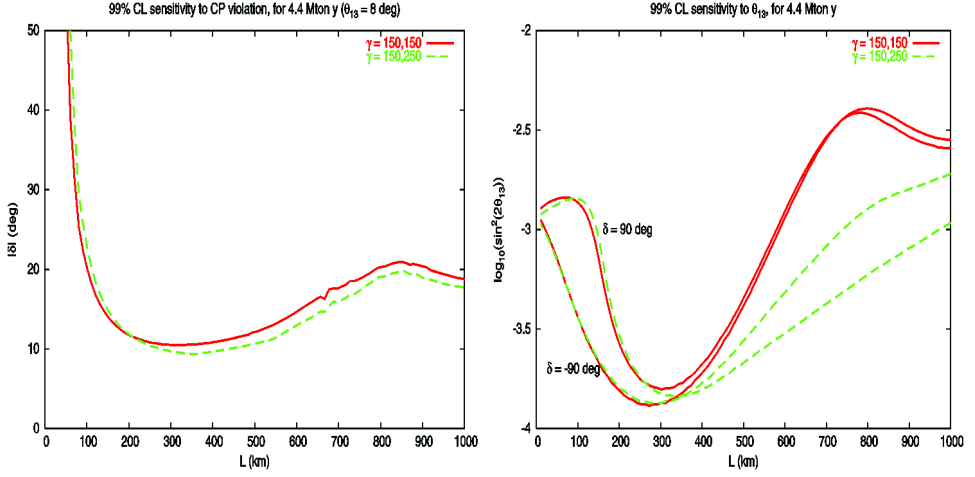


Fig. 9. Left: minimum value of $|\delta|$ distinguishable from 0 and 180° at 99% CL (for $\theta_{13} = 8^\circ$) versus the baseline for $\gamma = 150/150$ (solid) and $\gamma = 150/250$ (dashed). Right: minimum value of θ_{13} distinguishable from 0 at 99% CL versus the baseline for the same setups and for $\delta = 90^\circ$ and -90° as shown.

Fig. 9 shows the $|\delta|$ and θ_{13} sensitivities as a function of the baseline for $\gamma = 150/150$ and the asymmetric case $\gamma = 150/250$. The best CP sensitivity is achieved around $L \simeq 300$ (350) km for symmetric (asymmetric) beams.³ The baseline dependence of θ_{13} sensitivity leads to similar conclusions, although the importance of choosing the optimum baseline is more pronounced. A significant loss of θ_{13} sensitivity results if the baseline is too short, as in setup I.

Setup II will hence be defined as $\gamma = 150/150$ for $L = 300$ km. Similar results are expected for the asymmetric option $\gamma = 150/250$ with slightly longer baseline.

5. Comparison of the three setups

From the results of the previous section, the default setups to be compared are:

- Setup I: $\gamma_{\text{He}} = \gamma_{\text{Ne}} = 120$ at $L = 130$ km;
- Setup II: $\gamma_{\text{He}} = \gamma_{\text{Ne}} = 150$ at $L = 300$ km;
- Setup III: $\gamma_{\text{He}} = \gamma_{\text{Ne}} = 350$ at $L = 730$ km.

For the highest γ option, we have also checked that the symmetric and asymmetric options give comparable results.

³ The optimal baseline will obviously shift if Δm_{23}^2 is varied from the present best fit value: ± 50 km for a change of one σ .

5.1. Intrinsic sensitivity to θ_{13} and δ

Fig. 10 compares the CP violation and θ_{13} exclusion plots for the three setups assuming, for the moment, that the discrete ambiguities in $\text{sign}(\Delta m_{23}^2)$ and $\text{sign}(\cos \theta_{23})$ can be ignored because correct assignments have been made. Also included for reference is the previously considered setup from [32]. Although the highest γ option of [26] remains best, the performance of setup II is comparable. Even the sensitivity of the much-improved CERN–Frejus scenario in setup I is considerable. Although only the range $(-90^\circ, 90^\circ)$ is shown, to make it easier to read the y-scale, the region around 180° has a similar pattern.

As explained in [26], differences between the setups arise due to sample size (which increases at least linearly with γ) and more robust energy reconstruction at higher energies (as Fermi motion becomes less important).

Fig. 11 shows typical fits for the three setups at several *true* values of θ_{13} and δ . While both setups II and III manage to resolve the intrinsic degeneracy essentially everywhere in the sensitivity range, this is not the case for setup I; there (when the fake solution gets closer to and merges with the true one) the errors in θ_{13} and δ are sometimes strongly enhanced by the intrinsic degeneracy. This effect is not necessarily noticeable in the exclusion plot for CP violation.

5.2. Effect of the eight-fold degeneracies

By the time any β -beam begins, it is probable that a number of uncertainties in the oscillation parameters besides θ_{13} and δ will remain, in particular the discrete ambiguity in

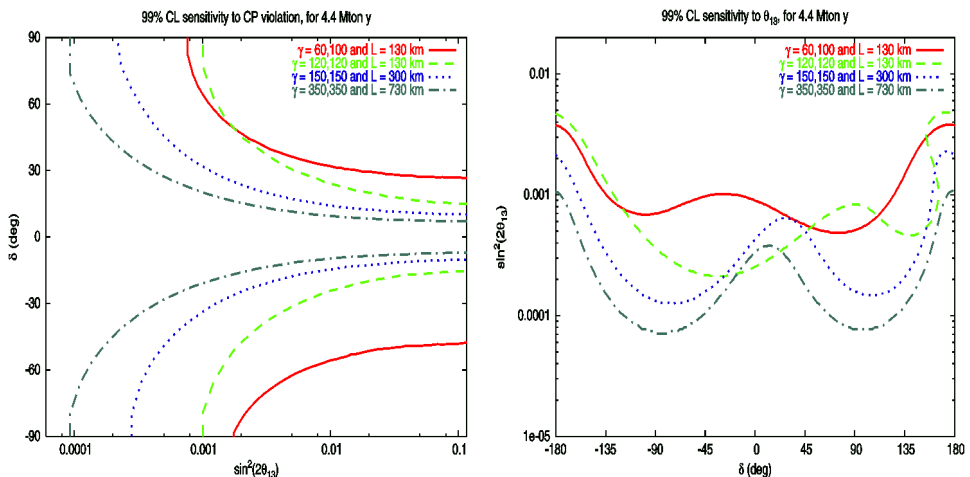


Fig. 10. Left: CP-violation exclusion plot at 99% CL for the three reference setups I (dashed), II (dotted) and III (dash-dotted) compared with the *standard* (solid) one of [15,32]. Right: exclusion plot for θ_{13} at 99% CL with the same setups. The solar and atmospheric parameters are fixed to their present best fit values and the discrete ambiguities are assumed to be resolved.

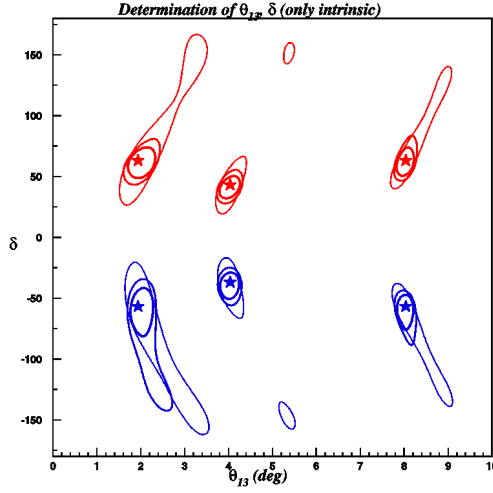


Fig. 11. Determination of (θ_{13}, δ) at 99% CL for setups III (thicker line), II (intermediate) and I (thinner line) and six different true values of the parameters indicated by the stars, assuming the correct $\text{sign}(\Delta m_{23}^2)$ and $\text{sign}(\cos \theta_{23})$.

$\text{sign}(\Delta m_{23}^2)$ ⁴ or the octant of θ_{23} . Both questions are theoretically important and the possibility of answering them with a β -beam is attractive. These ambiguities are problematic, if they cannot be resolved, because they can bias the determination of the parameters (θ_{13}, δ) , that is, the solutions surviving with the wrong assignment of the sign and/or the octant lie at different values of θ_{13} and δ than the true ones.

Generically, an eight-fold degeneracy of solutions appears when only the golden channel is measured and no energy dependence is available. There are two solutions in the absence of the discrete ambiguities, the true and the intrinsic one [17]. Each gets an false image for the wrong assignment of the sign [18], for the octant [19,20] and for both.

As explained in [23], the intrinsic solution and its three images are strongly dependent on the neutrino energy and therefore can be excluded, in principle, when the energy dependence of the oscillation signal is significant. On the other hand images of the true solution are energy independent and impossible to resolve unless there are additional measurements (e.g., disappearance measurements or the silver channel), or when there are significant matter effects.

Fig. 12 shows fits including the discrete ambiguities on the plane (θ_{13}, δ) for the three setups and different choices of the true θ_{13} and δ . In setup I we generically find the full eight-fold degeneracy, while in setups II and III the intrinsic solution and its images are typically excluded, thanks to the stronger energy dependence.

⁴ In this paper we considered the sign ambiguity as that of $\text{sign}(\Delta m_{23}^2)$, which involves a small change of the absolute 13 mass-splitting. Had we considered the discrete ambiguity as the change $\Delta m_{23}^2 \rightarrow -\Delta m_{13}^2$, the conclusions would not change, although the sensitivity to this discrete ambiguity would be slightly poorer in setup II.

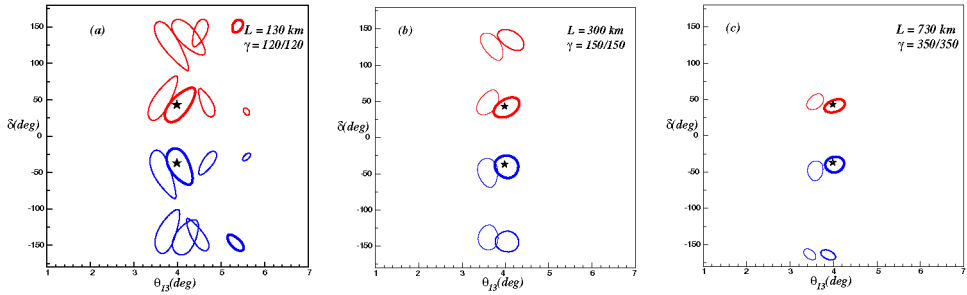


Fig. 12. Solutions for (θ_{13}, δ) for the true values: $\delta = \pm 40^\circ$ and $\theta_{13} = 4^\circ$ in (a) setup I, (b) setup II and (c) setup III. The contours correspond to the intrinsic ambiguity, the wrong sign, the wrong octant and the mixed, ordered from thicker to thinner-line contours.

Some general observations concerning these results include:

- Presence of the intrinsic degenerate solution or its images as in setup I is problematic, because it implies a significant increase in the measurement errors of θ_{13} and δ (as shown in Fig. 11) for some values of δ .
- When only the images of the true solution survive, as in setups II and III, they interfere with the measurement of θ_{13} and δ by mapping the true solution to another region of parameter space. In vacuum we find approximately [18,23]:
 Wrong-sign: $\theta_{13} \rightarrow \theta_{13}, \delta \rightarrow \pi - \delta$.
 Wrong-octant: $\theta_{13} \rightarrow \tan \theta_{23} \theta_{13} + \mathcal{O}(\Delta m_{12}^2)$, $\sin \delta \rightarrow \cot \theta_{23} \sin \delta$.
 Since these different regions occur for different choices of the discrete ambiguities they cannot fuse and one ends with a set of distinct measurements of θ_{13}, δ with different central values but similar errors (see the middle and right plots of Fig. 12).
- In vacuum, CP-violating solutions are mapped into CP-violating solutions, therefore the effects of degeneracies on the exclusion plot for CP violation are often small, even when degeneracies are a problem. In matter, on the other hand, the fake values of δ are modified by matter effects and for some central values of (θ_{13}, δ) the fake solutions may move closer to the CP-conserving lines than the true solution, resulting in an apparent loss of sensitivity to CP violation in some regions of the plane. This effect is visible in Fig. 12 where the fake-sign solution, which in vacuum should be located at $\sim -140^\circ$ for $\delta = -40^\circ$, gets shifted towards the CP-conserving line -180° for longer baselines, where matter effects are larger.

Figs. 13 and 14 show the range of (θ_{13}, δ) , where the $\text{sign}(\Delta m_{23}^2)$ and $\text{sign}(\cos \theta_{23})$ can be measured, respectively. Asymmetric γ options are also included, since there are some differences. As expected, sensitivity to the discrete ambiguities is better for large θ_{13} and larger γ . In setup I there is essentially no sensitivity anywhere on the plane.

Sensitivity to the discrete ambiguities and their bias in the determination of the parameters θ_{13} and δ could be significantly improved if data for any of the setups is combined with $\nu_\mu \rightarrow \nu_\mu$ disappearance measurements, for instance, in a superbeam experiment. This combination was recently studied in [33] for the *standard* β -beam with significant improvement in sensitivity to the mass hierarchy, even without matter effects. A similar study

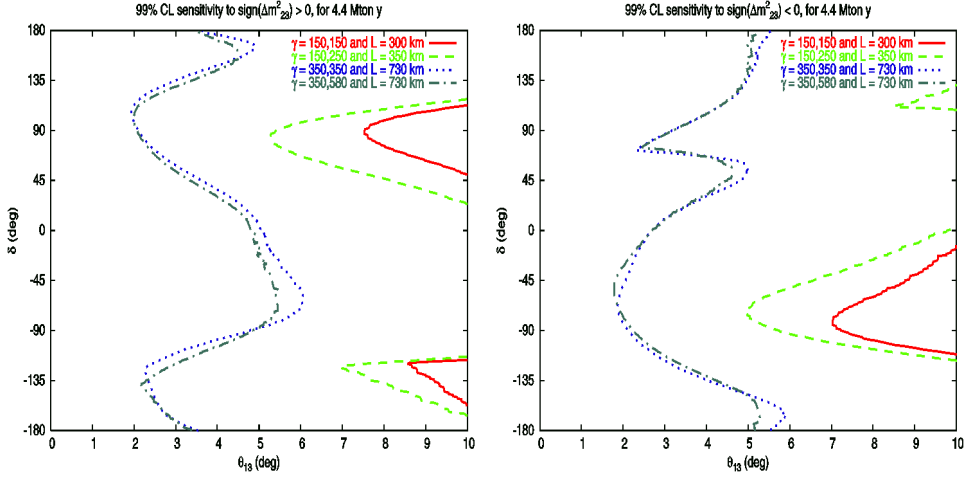


Fig. 13. Region on the plane (θ_{13}, δ) in which $\text{sign}(\Delta m_{23}^2)$ can be measured at 99% CL for the true $\text{sign}(\Delta m_{23}^2) = +1$ (left) and the true $\text{sign}(\Delta m_{23}^2) = -1$ (right), with $\theta_{23} = 40.7^\circ$. Symmetric and asymmetric beam options are shown for setup II: $\gamma = 150/150$ (solid) and $\gamma = 150/250$ (dashed), and setup III: $\gamma = 350/350$ (dotted) and $\gamma = 350/580$ (dashed-dotted). There is no sensitivity for setup I.

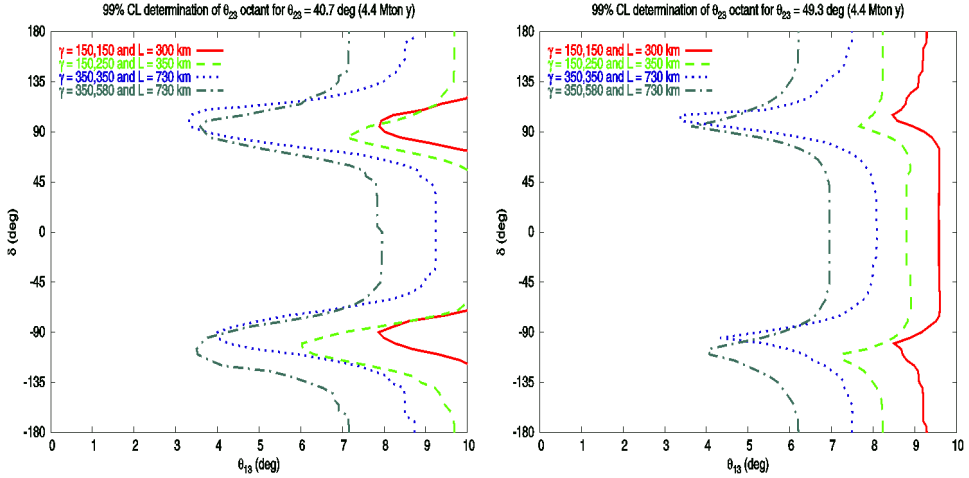


Fig. 14. Region on the plane (θ_{13}, δ) in which $\text{sign}(\cos \theta_{23})$ can be measured at 99% CL for $\theta_{23} = 40.7^\circ$ (left) and $\theta_{23} = 49.3^\circ$ (right). Symmetric and asymmetric beam options are shown for setup II: $\gamma = 150/150$ (solid) and $\gamma = 150/250$ (dashed), and setup III: $\gamma = 350/350$ (dotted) and $\gamma = 350/580$ (dashed-dotted). There is no sensitivity for setup I.

for the setups considered here will be very interesting. One of the most important limitations of the β -beam, compared to the superbeam or the neutrino factory, is its inability to measure the atmospheric parameters $(\theta_{23}, \Delta m_{23}^2)$ with precision. At the very least, information from T2K phase-I should be included, since otherwise the uncertainty on these

parameters will seriously compromise sensitivity to θ_{13} and δ . Synergies in resolving degeneracies, between the β -beam and T2K, should also be exploited.

Another interesting observation is that atmospheric neutrinos can be measured in the same megaton detector considered here. A recent study [34] combining atmospheric data with T2K phase-II has found a large improvement in sensitivity of the latter to both discrete ambiguities when θ_{13} is not too small ($> 4^\circ$). This is surely an analysis that should be done and will be reported elsewhere.

6. Conclusions

This paper has explored the physics potential of a CERN-SPS β -beam, where ions can be accelerated to $\gamma_{\text{He}} \leq 150$ and $\gamma_{\text{Ne}} \leq 250$. The design of a β -beam reaching this maximum γ is technically equivalent to the lower- γ option previously considered, for which a feasibility study already exists [28]. A major improvement in sensitivity to θ_{13} and δ is achieved by increasing γ . Even when the baseline is fixed to that of CERN–Frejus, sensitivity improves considerably with γ for $\gamma < 100$ and changes slowly as the γ increases further to the limit of the SPS.

An even more dramatic improvement is possible if the baseline is increased proportionally, so the first atmospheric oscillation maximum corresponds to the average neutrino energy, which occurs at $L \sim 300$ km. For large values of θ_{13} this option is comparable in CP-violation sensitivity to the optimal one in [26] at even higher $\gamma \sim \mathcal{O}(400)$, which would require a more powerful accelerator, such as the Tevatron or a refurbished SPS. In contrast, for small values of θ_{13} the latter option is still significantly better.

The main differences can be traced to increased event rate and the more significant energy dependence, which allows higher- γ options to resolve the intrinsic degeneracy.

For discrete ambiguities, higher- γ also provides a window on the neutrino mass hierarchy and the octant of θ_{23} , if non-maximal, relying on significant matter effects; the highest- γ setup with 730 km baseline is therefore the only one with a significant sensitivity.

In summary, if the existing CERN-SPS is the ion accelerator and the CERN–Frejus baseline is fixed, the γ considered in [15,32] should still be increased to a value ~ 100 or higher. If an alternative site hosts a large underground laboratory near CERN, it will be profitable to exploit longer baselines $L = 300$ km. In any case, R&D effort to design β -beams beyond the limit of the CERN-SPS appears justified, given the significant improvements in physics sensitivity they would allow.

Acknowledgements

We wish to thank A. Blondel, A. Donini, E. Fernández-Martínez, M.B. Gavela, M. Mezzetto and S. Rigolin for useful discussions. This work has been partially supported by CICYT (grants FPA2002-00612, FPA-2003-06921, FPA2004-00996), Generalitat Valenciana (GV00-054-1, GV2004-B-159), CARE-BENE (European Integrated Activity) and by the US Department of Energy grant DE-FG02-91ER40679.

Appendix A

The following tables include the migration matrices we have used for $\gamma = 120, 150$ and 350 for ${}^6\text{He}$ and ${}^{18}\text{Ne}$. Given an expected number of μ and e CC events in the true j th energy bin: \bar{n}_μ^j and \bar{n}_e^j , the observed number of muons n_μ^i in the reconstructed i th energy bin is obtained as:

$$n_\mu^i = \sum_j \epsilon_{ij}^{\text{app}} \bar{n}_\mu^j + \sum_j b_{ij}^{\text{app}} \bar{n}_e^j, \quad (\text{A.1})$$

Table 3

Efficiency ($\epsilon_{ij}^{\text{app}}$) and background (b_{ij}^{app}) migration matrices for the appearance signal at $\gamma = 120$ and 150. Each row and column of the matrices corresponds to a neutrino energy bin, as described in the text

Ion	γ	$\epsilon_{ij}^{\text{app}}$	b_{ij}^{app}
${}^6\text{He}$	120	$\begin{pmatrix} 0.65 & 0.18 & 0.071 \\ 0.03 & 0.54 & 0.33 \\ 0 & 0.016 & 0.34 \end{pmatrix}$	$\begin{pmatrix} 0.21 \times 10^{-3} & 0.30 \times 10^{-2} & 0.25 \times 10^{-2} \\ 0 & 0.68 \times 10^{-4} & 0.20 \times 10^{-3} \\ 0 & 0 & 0 \end{pmatrix}$
		$\begin{pmatrix} 0.47 & & 0.18 & 0.11 \\ 0.050 & & 0.34 & 0.23 \\ 0.77 \times 10^{-3} & 0.30 \times 10^{-1} & 0.14 \end{pmatrix}$	$\begin{pmatrix} 0.73 \times 10^{-3} & 0.20 \times 10^{-2} & 0.30 \times 10^{-2} \\ 0.12 \times 10^{-3} & 0.55 \times 10^{-3} & 0.11 \times 10^{-2} \\ 0 & 0.39 \times 10^{-4} & 0.74 \times 10^{-3} \end{pmatrix}$
${}^6\text{He}$	150	$\begin{pmatrix} 0.66 & 0.15 & 0.056 \\ 0.034 & 0.56 & 0.20 \\ 0 & 0.029 & 0.44 \end{pmatrix}$	$\begin{pmatrix} 0.22 \times 10^{-3} & 0.31 \times 10^{-2} & 0.24 \times 10^{-2} \\ 0 & 0.80 \times 10^{-4} & 0.12 \times 10^{-3} \\ 0 & 0 & 0 \end{pmatrix}$
		$\begin{pmatrix} 0.47 & & 0.16 & 0.082 \\ 0.054 & & 0.34 & 0.16 \\ 0.84 \times 10^{-3} & 0.04 & 0.23 \end{pmatrix}$	$\begin{pmatrix} 0.78 \times 10^{-3} & 0.22 \times 10^{-2} & 0.35 \times 10^{-2} \\ 0.12 \times 10^{-3} & 0.66 \times 10^{-3} & 0.64 \times 10^{-3} \\ 0 & 0.47 \times 10^{-4} & 0.80 \times 10^{-3} \end{pmatrix}$

Table 4

Efficiency matrices for the appearance signal for $\gamma = 350$

Ion	γ	$\epsilon_{ij}^{\text{app}}$
${}^6\text{He}$	350	$\begin{pmatrix} 0.56 & 0.15 & 0.068 & 0.020 & 0.010 & 0.0063 & 0.0021 \\ 0.039 & 0.46 & 0.15 & 0.054 & 0.022 & 0.011 & 0.0069 \\ 2.47 \times 10^{-4} & 0.042 & 0.37 & 0.14 & 0.060 & 0.019 & 0.013 \\ 0 & 2.22 \times 10^{-4} & 0.036 & 0.29 & 0.12 & 0.055 & 0.026 \\ 0 & 1.80 \times 10^{-4} & 9.74 \times 10^{-4} & 0.031 & 0.19 & 0.085 & 0.044 \\ 0 & 0 & 0 & 6.80 \times 10^{-4} & 0.026 & 0.16 & 0.091 \\ 0 & 0 & 0 & 4.69 \times 10^{-4} & 8.43 \times 10^{-4} & 0.018 & 0.15 \\ 0.34 & 0.14 & 0.065 & 0.023 & 0.012 & 0.012 & 0.0035 \end{pmatrix}$
		$\begin{pmatrix} 0.048 & 0.24 & 0.12 & 0.063 & 0.021 & 0.014 & 0.0072 \\ 0.0040 & 0.034 & 0.18 & 0.10 & 0.053 & 0.023 & 0.0093 \\ 4.22 \times 10^{-4} & 0.0046 & 0.028 & 0.14 & 0.085 & 0.054 & 0.018 \\ 1.26 \times 10^{-4} & 9.21 \times 10^{-4} & 0.0028 & 0.020 & 0.092 & 0.066 & 0.036 \\ 5.73 \times 10^{-5} & 2.99 \times 10^{-4} & 3.23 \times 10^{-4} & 2.49 \times 10^{-3} & 0.014 & 0.062 & 0.053 \\ 0 & 1.49 \times 10^{-4} & 3.91 \times 10^{-4} & 3.05 \times 10^{-4} & 0.0019 & 0.0099 & 0.061 \end{pmatrix}$

Table 5

Background matrices for the appearance signal for $\gamma = 350$

Ion	γ	b_{ij}^{app}
${}^6\text{He}$	350	$\begin{pmatrix} 8.66 \times 10^{-5} & 1.88 \times 10^{-4} & 7.27 \times 10^{-4} & 6.61 \times 10^{-4} & 1.78 \times 10^{-3} & 3.61 \times 10^{-3} & 1.89 \times 10^{-3} \\ 0 & 0 & 3.23 \times 10^{-4} & 0 & 2.08 \times 10^{-4} & 3.12 \times 10^{-4} & 6.65 \times 10^{-4} \\ 0 & 0 & 0 & 0 & 3.24 \times 10^{-4} & 0 & 0 \\ 0 & 0 & 0 & 0 & 0 & 0 & 2.76 \times 10^{-4} \\ 0 & 0 & 0 & 0 & 0 & 0 & 0 \\ 0 & 0 & 0 & 0 & 0 & 0 & 0 \\ 0 & 0 & 0 & 0 & 0 & 0 & 0 \\ 0 & 0 & 0 & 0 & 0 & 0 & 0 \end{pmatrix}$
		$\begin{pmatrix} 7.58 \times 10^{-4} & 6.81 \times 10^{-4} & 7.94 \times 10^{-4} & 1.08 \times 10^{-3} & 1.88 \times 10^{-3} & 1.10 \times 10^{-3} & 1.28 \times 10^{-3} \\ 5.30 \times 10^{-5} & 5.92 \times 10^{-4} & 2.48 \times 10^{-4} & 1.33 \times 10^{-4} & 1.76 \times 10^{-4} & 8.14 \times 10^{-4} & 9.63 \times 10^{-4} \\ 0 & 1.32 \times 10^{-4} & 2.59 \times 10^{-4} & 9.83 \times 10^{-4} & 2.37 \times 10^{-4} & 1.01 \times 10^{-4} & 0 \\ 0 & 1.48 \times 10^{-4} & 1.51 \times 10^{-4} & 1.95 \times 10^{-4} & 3.55 \times 10^{-4} & 0 & 0 \\ 0 & 0 & 0 & 0 & 0 & 0 & 0 \\ 0 & 0 & 0 & 0 & 2.17 \times 10^{-4} & 2.15 \times 10^{-4} & 0 \\ 0 & 0 & 0 & 0 & 0 & 0 & 0 \end{pmatrix}$

Table 6

Efficiency matrices ($\epsilon_{ij}^{\text{dis}}$) of the CC ν_e disappearance signal for different values of γ

Ion	γ	$\epsilon_{ij}^{\text{dis}}$
${}^6\text{He}$	120	$\begin{pmatrix} 0.89 & 0.25 & 0.10 \\ 0.04 & 0.62 & 0.40 \\ 0 & 0.023 & 0.38 \end{pmatrix}$
		$\begin{pmatrix} 0.83 & & 0.35 & & 0.21 \\ 0.073 & & 0.46 & & 0.36 \\ 0.15 \times 10^{-2} & & 0.43 \times 10^{-1} & & 0.22 \end{pmatrix}$
${}^6\text{He}$	150	$\begin{pmatrix} 0.89 & 0.21 & 0.086 \\ 0.045 & 0.63 & 0.25 \\ 0 & 0.041 & 0.52 \end{pmatrix}$
		$\begin{pmatrix} 0.83 & & 0.33 & & 0.16 \\ 0.078 & & 0.47 & & 0.27 \\ 0.19 \times 10^{-2} & & 0.059 & & 0.33 \end{pmatrix}$

Table 7

Efficiency matrices for the disappearance signal for $\gamma = 350$

Ion	γ	$\epsilon_{ij}^{\text{dis}}$
${}^6\text{He}$	350	$\begin{pmatrix} 0.64 & 0.19 & 0.061 & 0.021 & 0.014 & 0.011 & 0.0052 \\ 0.055 & 0.56 & 0.19 & 0.082 & 0.028 & 0.019 & 0.012 \\ 5.32 \times 10^{-4} & 0.061 & 0.49 & 0.19 & 0.082 & 0.029 & 0.017 \\ 0 & 0 & 0.049 & 0.41 & 0.20 & 0.096 & 0.047 \\ 0 & 4.17 \times 10^{-4} & 1.59 \times 10^{-3} & 0.037 & 0.37 & 0.19 & 0.071 \\ 0 & 0 & 0 & 0.0022 & 0.037 & 0.30 & 0.16 \\ 0 & 0 & 0 & 0 & 0.0031 & 0.052 & 0.32 \end{pmatrix}$
		$\begin{pmatrix} 0.47 & 0.24 & 0.12 & 0.040 & & 0.024 & & 0.013 & 0.0096 \\ 0.068 & 0.35 & 0.21 & 0.10 & & 0.040 & & 0.028 & 0.013 \\ 0.0071 & 0.055 & 0.27 & 0.18 & & 0.098 & & 0.054 & 0.022 \\ 8.09 \times 10^{-4} & 0.0046 & 0.052 & 0.24 & & 0.18 & & 0.084 & 0.046 \\ 2.74 \times 10^{-4} & 1.44 \times 10^{-3} & 5.91 \times 10^{-3} & 0.046 & & 0.22 & & 0.15 & 0.087 \\ 7.40 \times 10^{-5} & 1.90 \times 10^{-4} & 1.84 \times 10^{-3} & 3.44 \times 10^{-3} & & 3.86 \times 10^{-2} & & 0.17 & 0.15 \\ 8.60 \times 10^{-5} & 3.23 \times 10^{-4} & 8.43 \times 10^{-4} & 1.20 \times 10^{-3} & & 5.16 \times 10^{-3} & & 0.034 & 0.18 \end{pmatrix}$

while the observed electron events are:

$$n_e^i = \sum_j \epsilon_{ij}^{\text{dis}} \bar{n}_e^j, \quad (\text{A.2})$$

neglecting the background to the electron signal, which is negligible compared to the systematic errors discussed in Section 3.4.

References

- [1] Y. Fukuda, et al., Phys. Rev. Lett. 81 (1998) 1562, hep-ex/9807003.
- [2] S. Fukuda, et al., Phys. Rev. Lett. 86 (2001) 5651, hep-ex/0103032;
Q.R. Ahmad, et al., Phys. Rev. Lett. 89 (2002) 011301, nucl-ex/0204008;
Q.R. Ahmad, et al., Phys. Rev. Lett. 89 (2002) 011302, nucl-ex/0204009.
- [3] M. Apollonio, et al., Eur. Phys. J. C 27 (2003) 331, hep-ex/0301017;
K. Eguchi, et al., Phys. Rev. Lett. 90 (2003) 021802, hep-ex/0212021.
- [4] M.H. Ahn, Phys. Rev. Lett. 90 (2003) 041801, hep-ex/0212007.
- [5] Z. Maki, M. Nakagawa, S. Sakata, Prog. Theor. Phys. 28 (1962) 970.
- [6] S. Geer, Phys. Rev. D 57 (1998) 6989, hep-ex/0210192.
- [7] A. De Rújula, M.B. Gavela, P. Hernández, Nucl. Phys. B 547 (1999) 21, hep-ex/0210192.
- [8] For the extensive literature see, for example, the reviews M. Apollonio, et al., hep-ex/0210192;
J.J. Gómez-Cadenas, D.A. Harris, Annu. Rev. Nucl. Part. Sci. 52 (2002) 253, and the annual Proceedings of the International Nufact Workshop.
- [9] Y. Itow, et al., Nucl. Phys. B (Proc. Suppl.) 111 (2002) 146, hep-ex/0106019.
- [10] A. Para, M. Szleper, hep-ex/0110032;
D. Ayres, et al., hep-ex/0210005;
I. Ambats, et al., NOvA Collaboration, FERMILAB-PROPOSAL-0929.
- [11] B. Autin, et al., CERN/PS 2002-012.
- [12] H. Minakata, H. Nunokawa, Phys. Lett. B 495 (2000) 369, hep-ph/0004114;
J.J. Gómez-Cadenas, CERN working group on Super-Beams Collaboration, hep-ph/0105297;
H. Minakata, H. Nunokawa, JHEP 0110 (2001) 001, hep-ph/0108085;
P. Huber, M. Lindner, W. Winter, Nucl. Phys. B 645 (2002) 3, hep-ph/0204352;
G. Barenboim, et al., hep-ex/0206025.
- [13] V. Martemianov, et al., Phys. At. Nucl. 66 (2003) 1934–1939, Yad. Fiz. 66 (2003) 1982–1987 (in Russian), hep-ex/0211070;
H. Minakata, et al., Phys. Rev. D 68 (2003) 033017, hep-ph/0211111;
H. Minakata, et al., Phys. Rev. D 70 (2004) 059901, Erratum;
H. Minakata, et al., Phys. Lett. B 580 (2004) 216, hep-ph/0309323;
P. Huber, M. Lindner, T. Schwetz, W. Winter, Nucl. Phys. B 665 (2003) 487, hep-ph/0303232;
F. Ardellier, et al., hep-ex/0405032.
- [14] P. Zucchelli, Phys. Lett. B 532 (2002) 166.
- [15] M. Mezzetto, J. Phys. G 29 (2003) 1771, hep-ex/0302005;
M. Mezzetto, J. Phys. G 29 (2003) 1781, hep-ex/0302007.
- [16] A. Cervera, et al., Nucl. Phys. B 579 (2000) 17, hep-ph/0002108.
- [17] J. Burguet-Castell, et al., Nucl. Phys. B 608 (2001) 301, hep-ph/0103258.
- [18] H. Minakata, H. Nunokawa, JHEP 0110 (2001) 1, hep-ph/0108085.
- [19] G.L. Fogli, E. Lisi, Phys. Rev. D 54 (1996) 3667, hep-ph/9604415.
- [20] V. Barger, D. Marfatia, K. Whisnant, Phys. Rev. D 65 (2002) 073023, hep-ph/0112119.
- [21] V. Barger, D. Marfatia, K. Whisnant, Phys. Rev. D 66 (2002) 053007, hep-ph/0206038;
V. Barger, D. Marfatia, K. Whisnant, Phys. Lett. B 560 (2003) 75, hep-ph/0210428.
- [22] P. Huber, M. Lindner, W. Winter, Nucl. Phys. B 645 (2002) 3, hep-ph/0204352.

- [23] J. Burguet-Castell, M.B. Gavela, J.J. Gómez-Cadenas, P. Hernandez, O. Mena, Nucl. Phys. B 646 (2002) 301, hep-ph/0207080.
- [24] A. Donini, D. Meloni, P. Migliozzi, Nucl. Phys. B 646 (2002) 321, hep-ph/0206034; D. Autiero, et al., hep-ph/0305185.
- [25] D. Casper, Nucl. Phys. B (Proc. Suppl.) 112 (2002) 161, hep-ph/0208030.
- [26] J. Burguet-Castell, et al., Nucl. Phys. B 695 (2004) 297.
- [27] J.J. Gómez-Cadenas, in: Proceedings of the Neutrino Oscillation Workshop, NOW2004, Nucl. Phys. B (Proc. Suppl.), in press.
- [28] B. Autin, et al., CERN/PS 2002-078 (OP), in: Proceedings of the Nufact02, London 2002, J. Phys. G, in press, for more references see also: <http://beta-beam.web.cern.ch/beta-beam/>.
- [29] M. Lindroos, Talk at the Moriond Workshop on Radioactive beams for nuclear physics and neutrino physics, <http://moriond.in2p3.fr/radio/>.
- [30] M. Lindroos, private communication.
- [31] M. Goodman, et al., in: D. Casper, C.K. Jung, C. McGrew, C. Yanagisawa (Eds.), Physics Potential and feasibility of UNO, SBHEP01-3, July 2001.
- [32] J. Bouchez, M. Lindroos, M. Mezzetto, hep-ex/0310059.
- [33] A. Donini, E. Fernández-Martínez, S. Rigolin, hep-ph/0411402.
- [34] P. Huber, M. Maltoni, T. Schwetz, hep-ph/0501037.